Causes of plasma column contraction in surface-wave-driven discharges in argon at atmospheric pressure

Marco Antonio Ridenti,* Jayr de Amorim,† and Arnaldo Dal Pino
Department of Physics, ITA (Technological Institute of Aeronautics), São José dos Campos 12228-900, Brazil

Vasco Guerra
Instituto de Plasmas e Fusão Nuclear, Instituto Superior Técnico, Universidade de Lisboa, Avenida Rovisco Pais, 1049-001 Lisboa, Portugal

George Petrov
Naval Research Laboratory, Plasma Physics Division, 4555 Overlook Avenue SW, Washington, DC 20375, USA

(Received 4 October 2017; published 3 January 2018)

In this work we compute the main features of a surface-wave-driven plasma in argon at atmospheric pressure in view of a better understanding of the contraction phenomenon. We include the detailed chemical kinetics dynamics of Ar and solve the mass conservation equations of the relevant neutral excited and charged species. The gas temperature radial profile is calculated by means of the thermal diffusion equation. The electric field radial profile is calculated directly from the numerical solution of the Maxwell equations assuming the surface wave to be propagating in the TM_{00} mode. The problem is considered to be radially symmetrical, the axial variations are neglected, and the equations are solved in a self-consistent fashion. We probe the model results considering three scenarios: (i) the electron energy distribution function (EEDF) is calculated by means of the Boltzmann equation; (ii) the EEDF is considered to be Maxwellian; (iii) the dissociative recombination is excluded from the chemical kinetics dynamics, but the nonequilibrium EEDF is preserved. From this analysis, the dissociative recombination is shown to be the leading mechanism in the constriction of surface-wave plasmas. The results are compared with mass spectrometry measurements of the radial density profile of the ions Ar^+ and Ar_2^+. An explanation is proposed for the trends seen by Thomson scattering diagnostics that shows a substantial increase of electron temperature towards the plasma borders where the electron density is small.

DOI: 10.1103/PhysRevE.97.013201

I. INTRODUCTION

The phenomenon of the positive column's contraction of gas discharges has been observed and discussed for more than a century. It was described systematically for the first time by the German physicist Johannes Stark in his book *Elektrizität in Gasen* in 1902 [1]. In this book, he describes a typical discharge produced in a transparent vacuum tube using a dc power supply. He reported that the light emitted by the plasma's positive column did not always fill the whole tube volume. He noted that under low pressure the discharge filled all the tube's cross section but as the pressure was increased it would eventually collapse into a thin canal between the anode and cathode.

Although the first report of such phenomenon was more than a century ago, the contracted discharge regime did not receive as much attention as the discharge regime at lower pressures. The mathematical description of the low pressure regime was accomplished by Schottky in 1924 [2]. His theory described the radial profile of electrons and positive ions by assuming that charge production occurred by electron impact ionization and that charge loss occurred by diffusion into the walls. Unfortunately, the Schottky theory could not predict the contraction effect.

In contrast, convection or wall stabilized arcs at higher pressures could be successfully described assuming that volume recombination of charged particles was the only mechanism of loss. The intermediate case, where both diffusion and recombination contribute about equally, remained unsolved. This fact can be promptly illustrated if we consider that in 1954 Fowler reviewed four different theories to explain discharge contraction [3]. The author himself proposed a fifth one, in which it was suggested that inelastic collisions produce a damping effect, which accounted for the contraction effect by means of an antidispersing action. The author recognized that it was an oversimplification, but it was an attempt to account for the effect of inelastic collisions on the electron energy distribution function (EEDF). His theory was not fully accepted due to the lack or rigor based on kinetic theory.

The four explanations in Fowler's paper are now revisited because they offer a better understanding of the current status of the problem. The first explanation is based on the intrinsic nonlinearity of the differential equations that describe the transport of charge carriers. The conventional Schottky theory does not include them. One possible cause for nonlinearity arises from the mathematical formulation of the transport equations in the sheath region [4]. However, it can be dismissed on grounds that the contraction occurs when the pressure is

*marcoridenti@gmail.com
†jayr.de.amorim@gmail.com

increased, while the sheath length decreases with pressure. But other nonlinearities may play an important role. For instance, dissociative recombination reaction introduces rates in the mass conservation equations that depend on the square of the charge density.

The second group of explanations is related to the rate of volume recombination, in particular electron-ion recombination. This mechanism was thought to be too weak to explain the magnitude of the observed effect, until the dissociative recombination of molecular ions with electrons was discovered. This is because the rate coefficient for dissociative recombination is several orders of magnitude higher than the electron-ion recombination rate coefficient. Pioneering work by Kenty published in 1962 was the first to suggest the crucial role of dissociative recombination in the onset of plasma constriction [5]. Kenty went one step further by suggesting that it was related to the gas temperature gradient.

In fact, the third group of explanations attributed the onset of plasma contraction to temperature gradient, but they were not related to any kind of volume recombination. It was thought that the transport equations of mass, momentum, and energy could give rise to a solution that would eventually describe a thin channel of dense plasma surrounded by a hot neutral gas which transported heat outward [6]. The temperature gradient also implied a number density gradient, which could eventually produce a significant drop in the reduced electric field E/N in the outer regions of the plasma column and trigger the plasma contraction. At the time that this explanation was proposed no numerical solution could be found and all the reasoning was based on the equation's analysis in limiting cases. Today we know that the temperature and number density gradients may also influence the rate coefficients and reaction rates of important reactions, such as dissociative recombination. For that reason, the first and third explanations are usually grouped together and referred to as nonuniform gas heating effects. In spite of that fact, the role of gas heating and volume recombination should always be analyzed separately, since a model accounting for nonuniform gas heating alone may give completely different predictions when compared to an analysis which also includes volume recombination.

There was also an attempt to associate the contraction of the plasma column to the well known Z-pinch effect, but it was soon understood to be a poor explanation for the following reason. If we consider the typical electron temperatures and densities of these discharges, the confinement current computed using the Bennett relation would be something between 100 A and 1000 A [7], which is much higher than the actual currents observed in contracted columns ($\lesssim$0.01 A). Therefore, the Z-pinch effect does not play any role in these cases.

The numerous theories developed over the years could not be tested until the advance of computer technology that allowed the numerical study of this topic. Theoretical and numerical analysis made by Golubovskii and co-workers showed that in many cases the contraction effect may be explained solely by the dependence of the ionization rate with electron density, which is related to the competition of electron-atom and electron-electron collisions [8–12]. In argon and neon, for instance, this effect was proposed as the main explanation for plasma contraction. One of the main arguments supporting that conclusion was that experiments carried out with controlled wall temperature in argon and neon discharges would still contract, ruling out nonuniform gas heating. In contrast, the same experimental procedure did not lead to plasma contraction in helium, so in this case nonuniform gas heating was considered to be the primary mechanism of contraction.

Nonetheless, other numerical models which assume a Maxwellian EEDF everywhere in the plasma column could successfully predict the plasma contraction in argon discharges, as demonstrated by Moisan's group [13,14]. These models included detailed chemical kinetics, with dissociative recombination, and the heat equation to describe the nonuniform gas heating. The effect of the nonequilibrium EEDF was not taken into account; nonetheless, the model was able to describe the plasma contraction and explain experimental data. Whether or not this can be harmonized with Golubovskii's theory remains an open question.

To elucidate this issue we use a particular example in which we modeled an argon discharge at atmospheric pressure sustained by a surface wave at microwave frequency. Our approach is very similar to the ones proposed by Petrov and Ferreira [15] and Dyatko *et al.* [16], which consider a uniform electric field and dc current. In contrast, we solve the Maxwell equations that describe the TM_{00} field components of the surface wave, which were coupled to the transport equations. A very similar approach was adopted by Gregorio *et al.* to describe microplasmas produced by microwave sources [17]. This is a different problem because the magnitude of the electric axial field increases towards the tube wall to a maximum value near the boundaries.

We simplified the problem by neglecting the gradients in the axial direction, so that the equations could be written only in the radial coordinate. There are many works in the literature that consider the axial coordinate and the detailed geometry of the microwave launcher, but as far as we are concerned these works assume the EEDF to be Maxwellian [18,19]. Here the EEDF is calculated using the electron Boltzmann equation in the classical two-term expansion. In order to study the most important contributions to the contraction, we considered three scenarios. In the first scenario, the EEDF was calculated solving the Boltzmann equation. In the second scenario, the EEDF was considered to be Maxwellian, and in the third scenario the dissociative recombination was excluded from the chemical kinetics dynamics, but the nonequilibrium EEDF was preserved.

Our primary motivation was the theoretical interpretation of a recent experimental work based on mass spectrometry which reported measurements of the ionic fluxes of Ar^+ and Ar_2^+ as a function of the radial coordinate in a surface-wave discharge in argon at atmospheric pressure [20]. As we will show, the numerical results reproduced the experimental behavior of the ionic fluxes [20]. The trend of the experimental data was marked by the population inversion of the ions Ar^+ and Ar_2^+, the density of Ar^+ being higher in the center of the discharge and the density of Ar_2^+ being higher near the border. That result was consistent with Kenty's mechanism [5], which was the first explanation stating that dissociative recombination with molecular ions in the outer regions of the plasma was the main source of charge loss leading to contraction.

The results that we present here also shed light on the interpretation of electron temperature measurements of contracted surface-wave discharges carried out by means of Thomson scattering [21–23]. The experimental data show that the electron temperature increases significantly towards the border as the electron density decreases whenever the discharge is in the contracted regime. Here these measurements will be interpreted in light of the shape variation of the calculated EEDF at different radial positions. As will be shown, the experimental observations can only be correctly interpreted if the EEDF is nonequilibrium. We also discuss what is in our opinion the most accurate interpretation of the electron temperature measurements and how it is related to the temperature defined as $2/3\,\langle E\rangle$.

II. THEORY AND MODELING

A. Problem definition

Before proceeding with a detailed description of the model, we shall give an overall picture of the experimental setup. This is relevant because the simulation was run using physical parameters which were consistent with these experimental conditions. We recall that our primary motivation was to explain the mass spectrometric results from our previous work [20]. Many other works report data on the electron density and temperature radial profiles of similar discharges, and our model could be adapted to their particular experiments. However, we chose this particular condition, emphasizing the investigation of the contraction mechanism.

In this plasma source, the electromagnetic wave is excited by means of a surface-wave launcher called the surfatron, which is basically a cylindrical resonant cavity [24] which excites a surface wave along the plasma medium. The feeding gas is delivered through a ceramic tube with one millimeter radius, which is inserted into the launcher's central cavity. The tube's end is placed near the launcher gap, so that the plasma column extends into the ambient air. Although a small number of air molecules penetrates the flow, the density of these species is small relative to Ar. Here we use a pure Ar plasma chemistry scheme to approximately describe the plasma. The physical configuration of such system is visualized in Fig. 1.

The plasma column is assumed to have cylindrical symmetry. We take a slice that is orthogonal to the symmetry axis located at a distance Δz from the launcher gap and restrict our analysis to this slice. The results are expected to be valid as long as the axial gradients of the relevant physical quantities are much smaller than the radial gradients. In the next sections, we give a more detailed description of each part of the model and show how they are connected in the iterative self-consistent procedure.

B. Electron kinetics

The purpose of the electron kinetics study was the computation of the EEDF as a function of the radial coordinate, which is of fundamental importance for the calculation of many crucial plasma quantities such as the electron mean energy, the electron temperature, transport parameters, and reaction rate coefficients. These quantities are needed as input data in the modeling of plasma chemistry, plasma heating, and electrodynamics, which will be discussed in the next section.

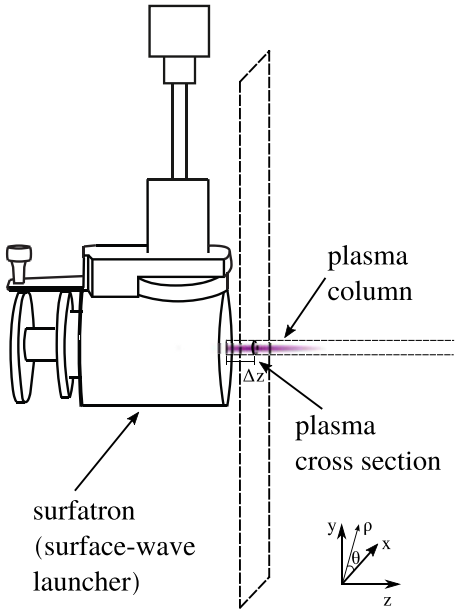

FIG. 1. Scheme of a typical experimental setup. The problem is solved for a given cross section in the axial direction for which the electron density at the axis is known. The cross section is specified by its distance $\Delta z = 3.7$ mm from the launcher gap.

The simplest approach concerning the EEDF is to consider it Maxwellian. In this case, an energy balance equation for the electrons is needed to calculate the temperature that characterizes its Maxwellian distribution. However, plasmas in rare gases at atmospheric pressure almost always have some degree of deviation from equilibrium [25], which requires numerical solution of the Boltzmann equation. This method was used for the first time by Morse *et al.* [26] back in the 1930s to study the EEDF of elastically colliding electrons in uniform electric fields and was further expanded to include the description of oscillating fields [27,28], inelastic collisions [28], and magnetic fields [29]. In the analysis developed by these authors the electron velocity distribution function (EVDF) is written as a spherical harmonics expansion in the velocity space. The z coordinate from which the polar angle is accounted for is usually set to the direction of the electric field. If the magnetic field is absent or can be neglected the problem becomes azimuthally symmetrical and the expansion reduces to a sum of Legendre polynomials of the polar angle's cosine. The first term of this expansion gives the EEDF [30] and it is isotropic in velocity space. The other terms are anisotropic and usually only the first of them is retained in the expansion. This technique, which is usually known as two-term expansion in the specialized literature, was adopted here. Some cases must be treated retaining higher order terms [31], but in the conditions met here, i.e., high-frequency Ar discharge subjected to low reduced electric fields, this approximation is considered to give a good description of the problem [32].

The steady-state electron Boltzmann equation may be written as [33–35]

$$\frac{d}{du}(G_E + G_c + G_{ee}) = \sqrt{\frac{2e}{m}} \sum_{s,j,j'} n_s[(u + u_{s,jj'})\delta_{s,j}\sigma_{s,jj'}(u + u_{s,jj'})f(u + u_{s,jj'}) - u\delta_{s,j}\sigma_{s,jj'}(u)f(u) - u\delta_{s,j'}\sigma'_{s,jj'}(u)f(u) + (u - u_{s,jj'})\delta_{s,j'}\sigma'_{s,jj'}(u - u_{s,jj'})f(u - u_{s,jj'})]. \quad (1)$$

The first term contains the electron fluxes in energy space due to the electric field (G_E), elastic collisions with heavy particles (G_c), and collisions between electrons (G_{ee}). These quantities depend only on the EEDF, $f(u)$, which is proportional to the anisotropic component of the EVDF. Their expressions are given by the following formulas:

$$G_E = -\frac{2e}{3m}\frac{E_{\text{eff}}^2 u^{3/2}}{\nu(u)}\frac{df}{du}, \quad (2)$$

$$G_c = -N\sqrt{\frac{2e}{m}}\left(\sum_s \frac{2m}{M_s}\delta_s\sigma_s^{m,e}\right)u^2\left(f + T_g\frac{df}{du}\right), \quad (3)$$

and

$$G_{ee} = -\sqrt{\frac{2}{m}}\frac{e^{5.5}}{8\pi\epsilon_0^2}n_e \ln\Lambda\left[I(u)f + J(u)\frac{df}{du}\right], \quad (4)$$

where

$$I(u) = \int_0^u f\sqrt{x}\,dx,$$

$$J(u) = \frac{2}{3}\left(\int_0^u f x^{3/2}dx + u^{3/2}\int_u^\infty f\,dx\right),$$

$$\ln\Lambda = \ln\left(12\pi n_e\lambda_D^3\right),$$

$$\nu(u) = \sqrt{\frac{2e}{m}}N\sum_s \delta_s u^{1/2}\sigma_s^m,$$

$$E_{\text{eff}} = \frac{E}{\sqrt{2}}\frac{1}{\sqrt{1 + \left(\frac{\omega}{\nu}\right)^2}}.$$

In Eqs. (1)–(4) u is the electron energy in eV; e and m are the elementary unit of charge and the electron mass, respectively; E is the maximum value of the high-frequency electric field; N is the absolute density of the gas; f is the EEDF satisfying the normalization condition $\int_0^\infty f(u)\sqrt{u}du = 1$; $\delta_s = n_s/N$ and $\delta_{s,j} = n_{s,j}/N$ are the relative densities of the atomic species s and of its excited electronic state j, respectively (n_s and $n_{s,j}$ being the corresponding absolute densities, satisfying $\sum_s n_s = N$ and $\sum_j n_{s,j} = n_s$); $\sigma_s^{m,e}$ and σ_s^m are the electron-neutral scattering cross sections for the elastic and the total momentum transfer, respectively; $\sigma_{s,jj'}$ and $\sigma'_{s,jj'}$ are the electron-neutral scattering cross sections for the excitation/deexcitation between upper level j' and lower level j of species s with energy threshold $u_{s,jj'}$; ϵ_0 is the vacuum permittivity; n_e is the electron density; λ_D is the Debye length; and ω is the angular frequency of the field. The quantities $\ln\Lambda$, ν, and E_{eff} are commonly known as Coulomb logarithm, electron collision frequency, and high-frequency effective field, respectively.

This stationary EBE (electron Boltzmann equation) was solved numerically using a standard finite difference procedure implemented in MATLAB. Many physical quantities such as the electric field, species densities, and gas temperature must be determined from equations which will be discussed in the next sections. These equations take the EEDF indirectly by its mean energy as an input parameter, so that a self-consistent scheme is needed. It also takes as input the cross sections for many different electron-neutral collisional processes which will be discussed in more detail in what follows. Before that, however, we shall explain the procedure for the special case where the EEDF is a Maxwellian distribution. In this case we determine the electron temperature from the energy balance equation. It can be derived from Eq. (1) by multiplying it by the kinetic energy and then integrating it in energy space to obtain

$$P_E = P_{\text{el}} + P_{\text{inel}}, \quad (5)$$

where P_E is the power gained from the applied electric field, P_{el} is the net power lost in elastic collisions, and P_{inel} is the net power lost in inelastic/superelastic collisions. They are given by the following expressions:

$$P_E = \int_0^\infty G_E\,du,$$

$$P_{\text{el}} = -\int_0^\infty G_{\text{el}}\,du,$$

$$P_{\text{inel}} = -\int_0^\infty \Theta_{\text{inel}}u\,du,$$

where Θ_{inel} is the right-hand term of Eq. (1). By determining the energy gain by the field and the energy lost in elastic and inelastic collisions, one is able to find the electron temperature T_e which satisfies Eq. (5) within an acceptable accuracy. Equation (5) was solved at each grid point to determine the radial profile of T_e. We shall mention that Eq. (5) does not contain the energy flux term, an approximation which is valid as long as the electron density variation is negligible in the energy relaxation length. The energy balance terms at a given axial position are determined only by the balance between the energy gained by the local field and the energy lost in collisions. This approximation is usually called the "local approximation." In cases for which the EBE was solved, the electron temperature is obtained from the EEDF as $2/3\langle u\rangle$. It also uses the local approximation assumption, though in this case the EEDF is computed instead of being assumed to be Maxwellian.

Table I shows the electronic collisional processes that participate in the numerical solution of the EBE. The cross sections were extracted from a database compiled by the plasma group from IST-Lisbon (Instituto Superior Técnico de Lisboa) which is available online in the LXcat project site [37]. Some processes do not have any perceptible effect on the EEDF, but their rate coefficients are needed in the computation of the balance equation of the heavy species. In such cases, the cross sections are computed using semiempirical formulas proposed by Vriens and Smeets [36] or the Klein-Roseland relation based on the microreversibility principle [38].

TABLE I. Electronic collisional processes included in the model and references for the cross-section databases. The tag EB indicates that the corresponding process was included in the EBE calculation, and the tag RC indicates that the rate coefficient was calculated for later use in the chemical kinetics code.

Collision	Aplication	Ref.	Threshold (eV)
Elastic:			
$Ar(^1S_0) + e \rightarrow Ar(^1S_0) + e$	EB	IST	
Excitation:[a]			
Excitation from $Ar(^1S_0)$:			
$Ar(^1S_0) + e \rightarrow Ar(^3P_1) + e$	EB, RC	IST	11.62
$Ar(^1S_0) + e \rightarrow Ar(^1P_1) + e$	EB, RC	IST	11.82
$Ar(^1S_0) + e \rightarrow Ar(^3P_2) + e$	EB, RC	IST	11.55
$Ar(^1S_0) + e \rightarrow Ar(^3P_0) + e$	EB, RC	IST	11.72
$Ar(^1S_0) + e \rightarrow Ar(4p) + e$	EB, RC	IST	13.00
$Ar(^1S_0) + e \rightarrow Ar^{**} + e$	EB	IST	14.00
Excitation from $4s$:			
$Ar(4s_i) + e \rightarrow Ar(4p) + e$	RC	IST	
Excitation between $4s$ states:			
$Ar(4s_i) + e \rightarrow Ar(4s_j) + e, i < j$	RC	IST	
Ionization:			
Ionization from $Ar(^1S_0)$:			
$Ar(^1S_0 + e \rightarrow Ar^+ + 2e$	EB, RC	IST	15.60
Ionization from $4s$:			
$Ar(4s_i) + e \rightarrow Ar^+ + 2e$	RC	[36]	
Ionization from $4p$:			
$Ar(4p) + e \rightarrow Ar^+ + 2e$	RC	[36]	2.60
Ionization from excimer Ar_2^*:			
$Ar_2^* + e \rightarrow Ar_2^+ + 2e$	RC	[36]	3.80
Superelastic processes:			
$Ar(4s) + e \rightarrow Ar(^1S_0) + e$	EB, RC	Klein-Rosseland	
$Ar(4p) + e \rightarrow Ar(^1S_0) + e$	EB, RC	Klein-Rosseland	
$Ar(4p) + e \rightarrow Ar\ (4s) + e$	RC	Klein-Rosseland	
$Ar(4s_i) + e \rightarrow Ar(4s_j) + e, i > j$	RC	IST	

[a]The electronic states of argon are expressed in L-S notation when upper cases are used. The minor case notation, such as $4s$ and $4p$, indicates the electronic configuration of the uppermost orbital and it is used to group together all states which share this configuration.

C. Treatment of ions and neutral species

The radial profile of the species densities may be computed using the mass conservation equations with a proper set of chemical reactions. We will not show here the detailed form of these equations, which may be found in many textbooks. In Ref. [39] these equations are written with special emphasis on problems of plasma modeling. Here we will limit ourselves to a detailed description of the set of chemical reactions and other processes that influence the particle balance, such as radiative decay and diffusion.

The mass conservation equation was solved for six neutral species: $Ar(^3P_2)$, $Ar(^1P_1)$, $Ar(^3P_0)$, $Ar(^3P_1)$, $Ar(4p)$, and Ar_2^*, and two charged species: Ar^+ and Ar_2^+. The electron density is determined as the sum of the positive species densities. The ten excited states in the electronic configuration $4p$ were grouped together and treated in the model as one excited level. Higher excited states of argon were not considered in this model. The same procedure was adopted in the case of the excimer Ar_2^*, which has a complex structure with singlet and triplet states, besides vibrational levels [40]. Therefore the detailed processes of the excimer kinetics were not taken into account.

For the density of the ground state $Ar(^1S_0)$ there is no need to solve the mass balance equation. Rather, it may be determined through the ideal gas law once the gas temperature is computed from the heat equation.

In order to solve the mass balance equations one needs to choose proper boundary conditions. The plasma's cross section (see Fig. 1) does not have boundaries and we assumed that all charged and radicals have null density at an imaginary border that we would get if the ceramic tube wall was prolongated downstream. This is an approximation, but it may give reasonable results since these species are supposed to be destroyed by the chemical processes in the surrounding air.

The system of the mass balance equations was solved numerically using the standard *pdepe* routine from MATLAB for parabolic partial differential equations. The time variable upper limit was chosen so that a stationary solution could be reached in that limit.

Table II lists the reactions involving other species. The rate coefficients were compiled from different references and in order to abbreviate the extensive work of detailing them we refer to previous works which adopted a very similar approach [41,42]. The reactions or rate coefficients which were introduced in this model will be discussed in what follows.

TABLE II. Reactions and other creation/destruction processes included in the mass balance equations of heavy species and their corresponding rate coefficients.

Reaction	Ref.	Reaction coefficient
Diffusion:		$[s^{-1}]$
Free diffusion:		
$Ar(^3P_2)$, $Ar(^3P_0)$	[42]	D_f/Λ^2
Ambipolar diffusion:		
Ar^+, Ar_2^+	[43]	D_a/Λ^2
Spontaneous emission:		$[s^{-1}]$
$Ar(^3P_1) \rightarrow Ar(^1S_0) + h\nu$	[44]	$g^{a} \times (1.19\times10^8)$, see text
$Ar(^1P_1) \rightarrow Ar(^1S_0) + h\nu$	[44]	$g^{a} \times (5.1\times10^8)$, see text
$Ar(4p) \rightarrow Ar(^3P_2) + h\nu$	[44]	1.43×10^7, see text
$Ar(4p) \rightarrow Ar(^3P_1) + h\nu$	[44]	7.3×10^6, see text
$Ar(4p) \rightarrow Ar(^3P_0) + h\nu$	[44]	3.5×10^6, see text
$Ar(4p) \rightarrow Ar(^1P_1) + h\nu$	[44]	9.83×10^6, see text
$Ar_2(*) \rightarrow 2Ar(^1S_0) + h\nu$	[40]	3.13×10^5, see text
Molecular conversion:		$[cm^6\ s^{-1}]$
$Ar^+ + Ar(^1S_0) + Ar(^1S_0) \rightarrow Ar_2^+ + Ar(^1S_0)$	[45]	$2.25\times10^{-31}(300/T_g)^{0.4}$
Dissociative recombination:		$[cm^3\ s^{-1}]$
$Ar_2^+ + e \rightarrow Ar(^1S_0) + Ar(^1S_0)$	[46]	$9.6\times10^{-7}[1-\exp(-\frac{630}{T_g})]\chi(\frac{300}{T_e})^{0.67}$, see text
Penning ionization:		$[cm^3\ s^{-1}]$
$Ar(4s_i) + Ar(4s_j) \rightarrow Ar(^1S_0) + Ar^+ + e$	[42]	$3.69\times10^{-11}T_g^{0.5}$
$Ar(4p) + Ar(4p) \rightarrow Ar^+ + Ar(^1S_0) + e$	[47]	5×10^{-10}
$Ar(4p) + Ar(4s) \rightarrow Ar^+ + Ar(^1S_0) + e$	[47]	5×10^{-10}
$Ar(4s_i) + Ar(4s_j) \rightarrow Ar_2^+ + e$	[47]	5×10^{-10}
Electronic impact dissociation:		$[cm^3\ s^{-1}]$
$e + Ar_2^+ \rightarrow e + Ar(^1S_0) + Ar^+$	[48]	$1.11\times10^{-6}\exp\{-\frac{[2.94-3(T_g[eV]-0.026)]}{(T_e[eV])}\}$
Atomic conversion:		$[cm^3\ s^{-1}]$
$Ar_2^+ + Ar(^1S_0) \rightarrow Ar^+ + 2Ar(^1S_0)$	[48]	$5.22\times10^{-10}\frac{\exp(-\frac{1.304}{T_g[eV]})}{T_g[eV]}$
Three-body recombination:		$[cm^6\ s^{-1}]$
$e + e + Ar^+ \rightarrow e + Ar(4p)$	[36]	$1.43\times10^{-28}(T_e[eV])^{-3}$
$e + e + Ar^+ \rightarrow e + Ar(^3P_2)$	[36]	$6.14\times10^{-29}(T_e[eV])^{-3}$
$e + e + Ar^+ \rightarrow e + Ar(^3P_1)$	[36]	$1.33\times10^{-29}(T_e[eV])^{-3}$
$e + e + Ar^+ \rightarrow e + Ar(^3P_0)$	[36]	$3.81\times10^{-29}(T_e[eV])^{-3}$
$e + e + Ar^+ \rightarrow e + Ar(^1P_1)$	[36]	$4.19\times10^{-29}(T_e[eV])^{-3}$
Excimer formation:		$[cm^6\ s^{-1}]$
$Ar(4s) + 2Ar(^1S_0) \rightarrow Ar_2(*) + Ar$	[41]	10^{-32}
Excimer extinction:		$[cm^3\ s^{-1}]$
$Ar_2(*) + Ar_2(*) \rightarrow Ar_2^+ + 2Ar(^1S_0)$	[40]	5×10^{-10}
$Ar_2(*) + Ar(4s) \rightarrow Ar_2^+ + Ar(^1S_0) + e$	[40]	6×10^{-10}
Atomic three-body recombination:		$[cm^6\ s^{-1}]$
$Ar^+ + Ar(^1S_0) + e \rightarrow 2Ar(^1S_0)$	[41]	$3.7\times10^{-29}T_e(eV)^{-1.5}T_g(K)^{-1}$

[a]Here g is the scape factor in Holstein's theory of radiative transport.

1. Diffusion

The diffusion processes are relevant in the case of the metastable $Ar(^3P_2)$ and $Ar(^3P_0)$ and the charged Ar^+ and Ar_2^+ species. In the first case, we adopted the diffusion coefficients of Kutasi and Guerra [42]. The ambipolar diffusion coefficients for the charged species were computed following Jonkers *et al.* [43] and the mobilities are from Ref. [49]. The electron diffusion and mobility were determined directly from the EEDF. The diffusion of resonant species was neglected since diffusive losses are negligible compared to radiative decay.

2. Spontaneous emission

The loss by spontaneous emission must be considered for all excited states, except metastables. The only species in the model that decay to the ground state are the excited states $Ar(^3P_1)$ and $Ar(^1P_1)$, for which cases it is important to take into account the radiation imprisonment due to the large density of atoms in ground state. This effect was taken into account using Holstein theory [50].

In the case of radiative decay from $4p$ states to $4s$ states it is important to consider the Einstein coefficients from the transition of each state k with configuration $4p$ to each state

i with configuration $4s$. Considering the statistical weights of each state, g_k, an effective decay coefficient from Ar($4p$) to each state i with configuration $4s$ was computed. The expression for this coefficient is

$$A_{4p,i} = \frac{\sum_k g_k A_{ki}}{\sum_k g_k}, \tag{6}$$

where the sum is taken over all the allowed transitions between the states with configuration $4p$ to each state with configuration $4s$. The values of the computed coefficients are shown in Table II.

The triplet state of the excimer has a non-negligible decay constant [40], though lower than the ones of other resonant species. Since the excimer does not exist in the fundamental state, there is no radiation imprisonment. However, the decay constant of the singlet state is much larger and because of that the density of the singlet is expected to be much lower than the density of the triplet. Therefore, we considered the decay constant of the triplet state as the effective decay constant of the excimer (see Table II).

3. Molecular conversion

The reaction of molecular conversion that forms the molecular ion Ar_2^+ is a three-body reaction, which plays an important role in rare gas discharges at atmospheric pressure. Unfortunately, the reaction rate coefficients from the literature are not perfectly adequate to plasma modeling, since the experiments from which they are determined are usually carried out at temperatures around 300 K. There are many studies with proposed values which are consistent among each other [45,51,52], but at low temperatures. Here we have adopted the rate coefficients from the work of Jones *et al.* [45] (see Table II).

4. Dissociative recombination

In this process an incident electron is captured by the ion, producing an autoionizing state $Ar_2^*(n)$ which dissociates into two neutral atoms. Since it is a very efficient process, it is usually the main channel of charge destruction. Although the rate coefficients have been studied experimentally by many authors [46,53], there is no reliable information concerning its branching ratio. It has been experimentally shown that two dissociation paths are possible: the formation of an atom in the ground state and another atom in one of the four states in the $4s$ electronic configuration or the formation of two atoms in the ground state [54]. Since it is an exothermic reaction, the extra energy is shared between the two atoms. The experimental study of Ramos *et al.* [54] showed that on average ~ 1.5 eV of the extra energy is carried by the $4s$ excited atom and the ground state. If the reaction occurs via the second path, ~ 7.21 eV is carried by the two atoms in the ground state. Since fast atoms are very likely to ionize due to collisions with other species, only a small proportion of the dissociative recombination effectively reduces the net charge of the discharge. Following Jonkers *et al.* [48], we considered that only 5% of the events effectively reduce the net charge of the plasma medium ($\chi = 0.05$).

5. Electronic impact dissociation

The process of electronic impact dissociation competes with dissociative recombination and the rate coefficients have the same order of magnitude at the typical plasma conditions of this study. In this process the incident electron excites the molecular ion from a bound state to an repulsive state which dissociates [55]. The rate coefficient for this process was extracted from the work of Jonkers *et al.* [48], which proposed an analytical expression consistent with the theoretical cross sections derived by Marchenko [55]. Even so, the dissociative recombination remains the main mechanism of charge destruction.

6. Three-body recombination

The three-body recombination processes are specially relevant to the charge balance when the electron density is relatively large ($n_e > 10^{15}$ cm^{-3}) or the molecular ion density is much smaller than the atomic ion density. The rate coefficient expression of the three-body recombination involving two electrons and an ion was taken from the work of Vriens and Smeets, which arrived at their expression using the microreversibility principle and their semiempirical formulas of the direct process (ionization). We also considered the three-body recombination processes involving the atom in the ground state as a third particle. In this case, the rate coefficient was taken from Ref. [41].

In order to guarantee the model consistency, we considered the recombination processes which are the inverse of the ionization of states $4s$ and $4p$ by electronic impact. Recombination to the ground state is negligible and it was not included in the model, since the ionization from the ground state is also negligible at the typical plasma conditions of this study. This was confirmed by the results as will be shown later. The excited states of the higher levels which were not considered in the model were considered to be at Saha equilibrium so that the ionization is compensated by the three-body recombination.

D. Plasma heating

The temperature was determined using the following heat equation:

$$\frac{1}{r}\frac{d}{dr}\left[r\lambda(T_g(r))\frac{dT_g}{dr}\right] = -\sigma_e(r)E_0(r)^2, \tag{7}$$

where $\lambda(T)$ is the thermal conductivity of argon, which is temperature dependent, and σ is the electric conductivity ($\sigma_e = en_e\mu_e$). Note that all the energy given up by the electrons to the plasma (Joule heating) contributes to plasma heating, not only elastic collisions. It is assumed that excited states convert the internal energy into translational energy mainly by relaxation processes, heating the gas. Equation (7) is frequently referred to as the Elenbaas-Heller equation [56], with an additional term accounting for the radiative losses. The terms containing axial gradients were also neglected, in accordance with earlier assumptions.

The thermal conductivity in Eq. (7) depends on the temperature, so an empirical relation for $\lambda(T)$ [57] had to be used to obtain a realistic solution. The electron conductivity $\sigma(r)$ was obtained from the solution of the electron Boltzmann equation. The electric field in the heat equation was determined

by solving the Maxwell equation, as will be described in the next section.

In the same way as the continuity equations, the heat equation was solved numerically using the standard *pdepe* routine from MATLAB for parabolic partial differential equations.

E. Plasma electrodynamics

Plasmas can be sustained by microwaves by several mechanisms. In the problem described here, the plasma is sustained by a propagating wave in the magnetic mode TM_{00}. Note that the discharge is also the propagating medium of the wave.

In the case of a TM_{00} propagating wave, the electric and magnetic fields **E** and **B** can be written in cylindrical coordinate as $\mathbf{E} = (E_r, 0, E_z)$ and $\mathbf{B} = (0, B_\phi, 0)$. These components are assumed proportional to the factor $\exp[-j\omega t + j\int_z k(z')dz']$, where $k = \beta + j\alpha$, β is the propagation coefficient, and α is the space damping factor (attenuation coefficient), and another factor which only depends on the radial coordinate. The relation between these components can be found using the Maxwell equations [58]

$$\frac{\partial B_\phi}{\partial z} = j\frac{\omega}{c^2}\epsilon E_r, \quad \frac{1}{r}\left[\frac{\partial}{\partial r}(rB_\phi)\right] = -j\frac{\omega}{c^2}\epsilon E_z,$$
$$\frac{\partial E_r}{\partial z} - \frac{\partial E_z}{\partial r} = j\omega B_\phi, \tag{8}$$

where ϵ is the medium relative dielectric constant. In the case of vacuum (or free space), the value is $\epsilon_0 = 1$; in the case of a dielectric, the value is ϵ_d; and in the case of a plasma the dielectric constant is given by the following formula [59]:

$$\epsilon_p = 1 - \frac{\omega_p^2}{\omega^2 + \nu^2} + j\frac{\nu}{\omega}\frac{\omega_p^2}{\omega^2 + \nu^2} = 1 - \xi + j\frac{\nu_1}{\omega}\xi, \tag{9}$$

where $\omega_p = (\frac{n_e e^2}{\epsilon_0 m_e})^{1/2}$ is the plasma oscillation frequency. After some algebraic manipulations of Eqs. (8), we arrive at the following expression for the component E_z:

$$\frac{1}{r}\left[\frac{\partial}{\partial r}\left(r\frac{\partial E_z}{\partial r}\right)\right]\left[\frac{k^2}{\kappa_p^2} - 1\right] + \frac{\partial E_z}{\partial r}\frac{\partial}{\partial r}\left(\frac{k^2}{\kappa_p^2}\right) = \frac{\omega^2}{c^2}\epsilon E_z, \tag{10}$$

where $\kappa_p = k^2 - (\omega^2\epsilon)/c^2$. We note that the solutions of Eq. (10) are complex, so that the physical solution is obtained taking the real part of the solution. Note also that the factor $\exp[-j\omega t + j\int_z k(z')dz']$ may be canceled out from Eq. (10) so that only the radial dependence is retained.

The propagating and attenuation coefficients must be determined from the continuity of the axial components of the electromagnetic fields in the boundary between the plasma and the air. Here we considered that the boundary is located at $r = R$, where R is the radius of the ceramic tube. We shall recall that our analysis is restricted to a given cross section of the plasma column propagating in the ambient air, so only the continuity relations in the boundary between the plasma and the air are needed. In order to solve that problem, we built a routine that searched for the attenuation and propagating coefficients which would satisfy the continuity relations. Equation (10) was solved numerically by means of the *ode45* solver from the MATLAB library of ordinary differential equations routines.

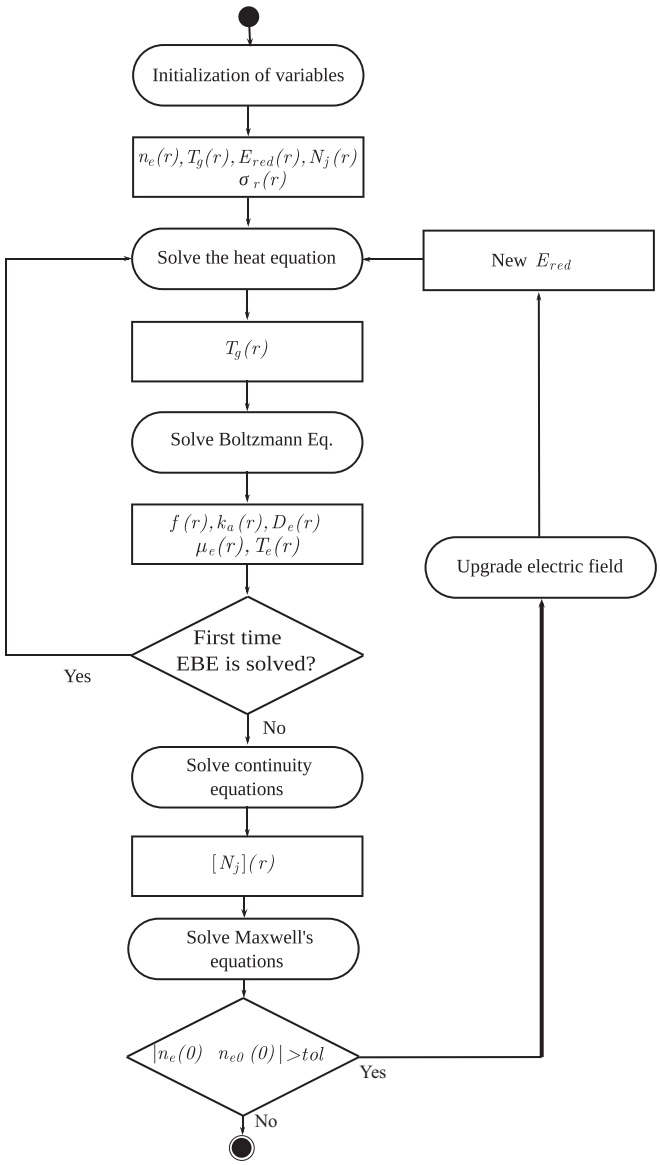

FIG. 2. Flow chart representing the self-consistent routine. Some of the symbols were not introduced in the text, namely, D_e, the electron free diffusion coefficient; N_j, the density of the heavy species j; and k_a, the rate coefficient of the electronic collisional processes.

F. Self-consistent method

The workflow of the self-consistent routine is sketched in Fig. 2. The variables—such as electron and ion densities, gas temperature, axial electric field, and transport parameters—were initialized using arbitrary profiles. The only fixed value was the electronic density at the center of the discharge, $n_{e0}(0)$, whose value was chosen equal to the one which was derived from line broadening measurements of the discharge in the desired condition [60]. The method consists of finding a solution for the radial profiles of all the relevant physical quantities which is consistent with the value $n_{e0}(0)$ at the column center. It may be thought as an eigenvalue problem, akin to that of Ref. [41]. For instance, the magnitude of the electric field E_z at the center is adjusted self-consistently with the radial profiles of the electric field and the charged and

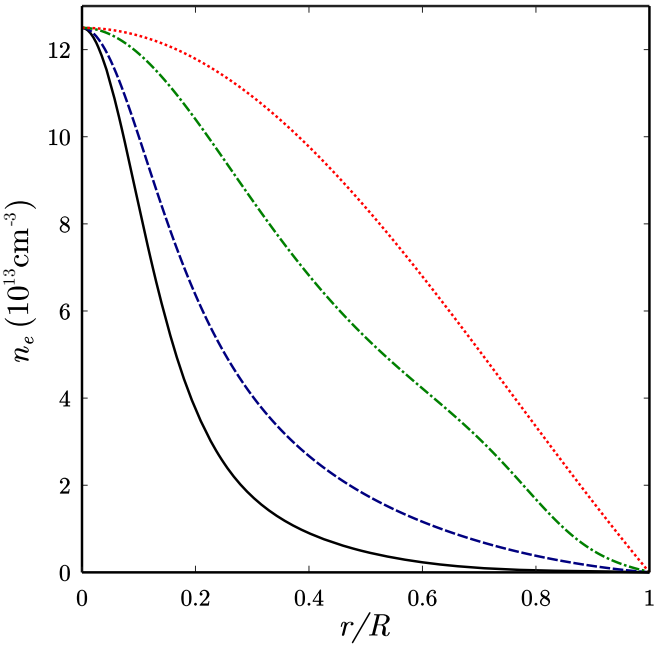

FIG. 3. Electron density profile. Three different scenarios are shown, namely, full model, with no restrictions (black solid line), Maxwellian EEDF (blue dashed line), no dissociative recombination (green dot-dashed line), and the Bessel profile (red dotted line).

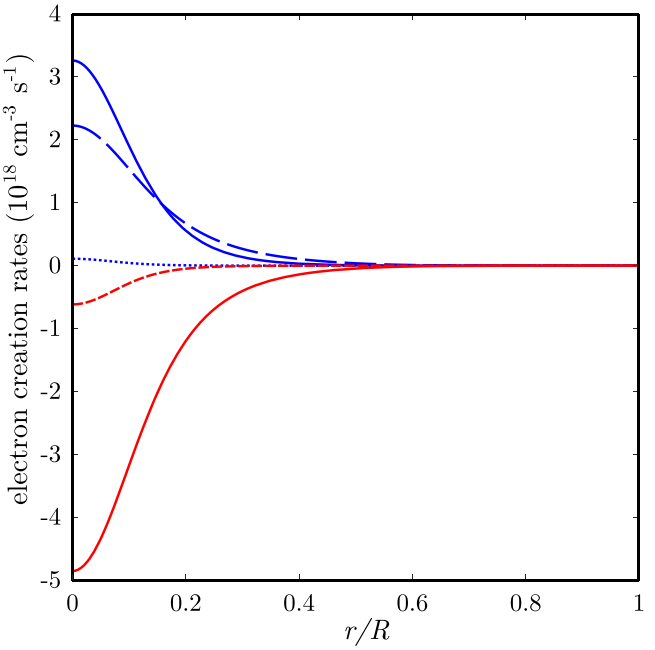

FIG. 4. Reaction rates of charge creation as a function of the normalized radial coordinate. The creation processes are shown in blue, where the solid line is the ionization from the 4s states, the long-dashed line is the ionization from the molecular argon excimer, and the dotted line is the ionization from the 4p states. The destruction processes, here shown as negative creation processes, are given by the red lines, where the solid line is the dissociative recombination and the short-dashed line is the atomic three-body recombination. These results were generated using the full model.

neutral particles which satisfy simultaneously the Maxwell equations and the mass conservation relations. This procedure is repeated iteratively until an electric field which is consistent with the electron density is found. The self-consistent routine described in the flow chart from Fig. 2 was implemented in MATLAB.

III. RESULTS AND DISCUSSION

A. Plasma contraction

The first result we show here is the electron density profile for three different modeling assumptions (see Fig. 3). The first condition is just the full model described earlier, without any simplification besides the ones we have already mentioned. In the second case we use a Maxwellian EEDF, as also described in the previous section. In the third case we have only omitted the dissociative recombination from the full model, keeping the nonequilibrium EEDF. We also plotted the Bessel profile which corresponds to the analytical solution of the density profile in the linearized Schottky model.

The value of the electron density at the center of the discharge was fixed at 1.25×10^{14} cm^{-3}. This value was estimated by means of the hydrogen Balmer series H_β line's broadening measured in the same experimental conditions of the mass spectrometric diagnostics (see Sec. III B 1), with the optical fiber fixed at $\Delta z = 3.7$ mm from the launcher exit. The results are presented as a function of the normalized radial coordinate r/R, where R is the tube radius with a diameter of 1.0 mm.

It can be clearly seen that the highest degree of contraction was obtained when the full model was considered. When the Maxwellian EEDF is assumed instead of the nonequilibrium one, we observed a relatively small broadening of the profile. The broadening was much more pronounced in the case where the dissociative recombination was switched off. These results suggest that the main mechanism leading to the discharge contraction is the dissociative recombination associated with the nonuniform heating, as postulated by Kenty's mechanism. The EEDF does play a significant role in the contraction phenomena, as can be clearly seen in the broadening of the profile in the second scenario. Nonetheless this broadening is small when compared to that in the third scenario and we may safely conclude that the dissociative recombination plays a more important role than the tail depletion and other EEDF related effects.

So how can this be reconciled with those experimental observations in which contraction was not prevented when the discharge tube was heated [11]? First of all, we must consider that temperature uniformity does not guarantee that dissociative recombination will not grow faster than ionization processes, even if the EEDF is Maxwellian. Besides that, the experimental method of heating the discharge tube cannot guarantee that the temperature will be radially uniform, because the intrinsic plasma heating, the initial feeding gas temperature, and its thermal conductivity may still contribute to the onset of non-negligible thermal gradients which may trigger discharge contraction due to Kenty's mechanism. For instance, helium has a much higher thermal conductivity than

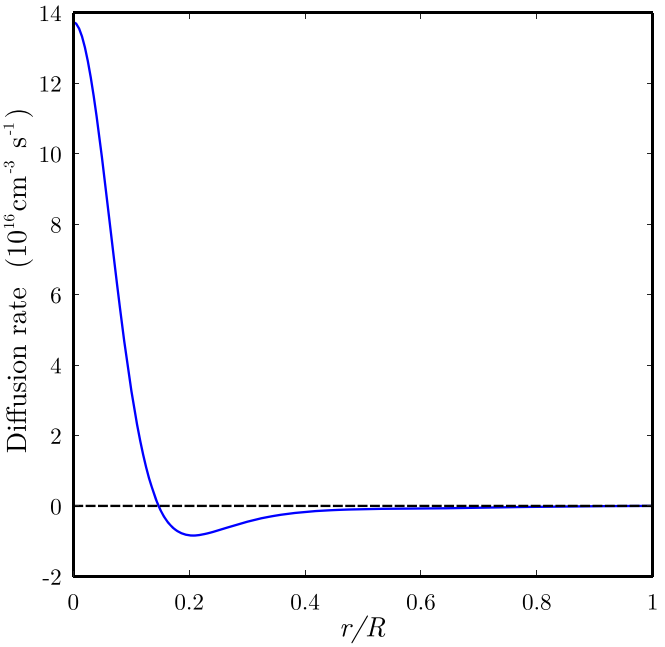

FIG. 5. Diffusion rate of charges as a function of the relative radial coordinate. These results were generated using the full model.

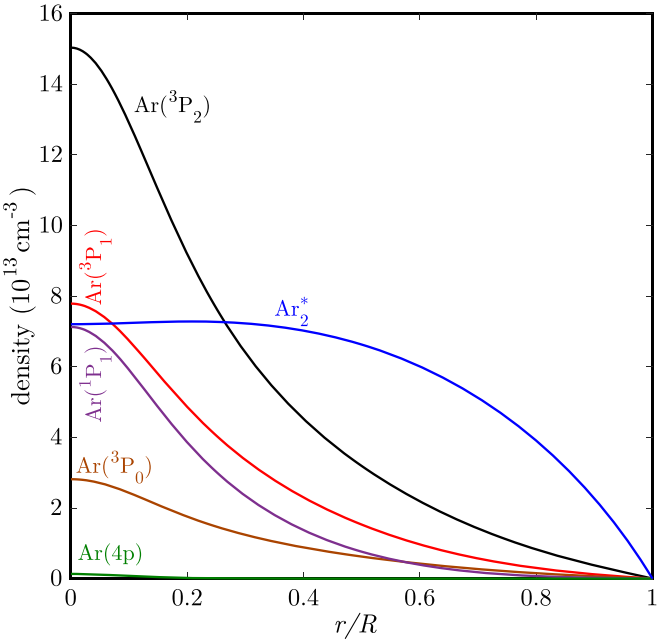

FIG. 6. Radial profile of the densities of the excited species considered in the model [$\mathrm{Ar}(^3P_2)$, $\mathrm{Ar}(^1P_1)$, $\mathrm{Ar}(^3P_0)$, $\mathrm{Ar}(^3P_1)$, $\mathrm{Ar}(4p)$, and Ar_2^*]. These results were generated using the full model.

argon and neon, which could also explain why the tube heating method only prevents the helium contraction.

In order to get a better understanding of the results from the full model, let us analyze the main contributions to the processes of charge creation and destruction. The plot in Fig. 4 shows the reaction rate of such processes as a function of the normalized radial coordinate. The plot in Fig. 5 shows the net effect of creation and destruction of charges and according to the particle balance equation it is equal to the diffusion rate in the stationary regime. We see in Fig. 4 that the most important creation process in the discharge center is the ionization from the $4s$ states. At the borders ($r/R > 0.2$) ionization from the excimer exceeds ionization from the $4s$ states. This is related to the radial profile of the density of the excimer, which is broader than the radial profiles of the $4s$ resonant and metastable states (see Fig. 6). The third most important creation process is the ionization from the $4p$ states. Note that the ionization from the ground state is not shown in the plot, because its contribution is negligible relative to the other creation processes.

The destruction of charges is caused mainly by the effect of dissociative recombination within the whole interval between $r/R = 0$ and $r/R = 1$. The atomic three-body recombination is also important, but always lower than the dissociative recombination. The plot of the diffusion rate in Fig. 5 shows that the net rate of charge creation is positive in the center of the plasma column ($r/R < 0.15$), but negative in the border. The equality between diffusion rate and charge creation/destruction rates imposed by the electron particle balance equation also implies that the diffusion must be positive in the center and negative at the border. The positive value corresponds to the typical behavior which is expected from the linearized Schottky model, where the charge produced in the discharge always diffuses towards the border. When the contraction phenomena takes place one observes a negative diffusion rate in the border and this effect is closely related to the contraction phenomena. Since the net creation of charge is negative in that region, the electron's flow through the inward radial surface of a fixed small cylindrical volume is higher than the flow through the outward radial surface. The destruction processes are acting analogously to a "charge filter" causing the abrupt collapse of the discharge column.

B. Consistency with experiment

1. *Mass spectrometric data of* Ar^+ *and* Ar_2^+

One of the main motivations for the modeling effort reported in this work was to obtain a theoretical description of the experimental observation of the radial profile of the Ar^+ and Ar_2^+ densities. These measurements were accomplished by means of mass spectrometry. More information concerning the experimental setup may be found elsewhere [20,61,62]. We also note that the raw data from mass spectrometry measurements are proportional to the particle flux. However, we are interested in the particle density. The procedure to convert the flux proportional measurements into density proportional values is described in detail in [62] and it is based on the supplementary information about the ion energy distribution, which was also determined experimentally.

The modeling results give a good qualitative description of the experimental data (see Fig. 7). The inversion of the $[\mathrm{Ar}^+]/[\mathrm{Ar}_2^+]$ ratio is observed both experimentally and theoretically around $r/R \approx 0.25$. Nonetheless, the full model's results overestimate the $[\mathrm{Ar}^+]/[\mathrm{Ar}_2^+]$ ratio in the column center. Besides that, the $[\mathrm{Ar}^+]$ profile seems to be too narrow. On the other hand, the model which assumes a Maxwellian EEDF seems to predict correctly the column's center $[\mathrm{Ar}^+]/[\mathrm{Ar}_2^+]$ ratio, but the profile in this case is clearly too broad. On the theoretical side, we must take into account many uncertainties

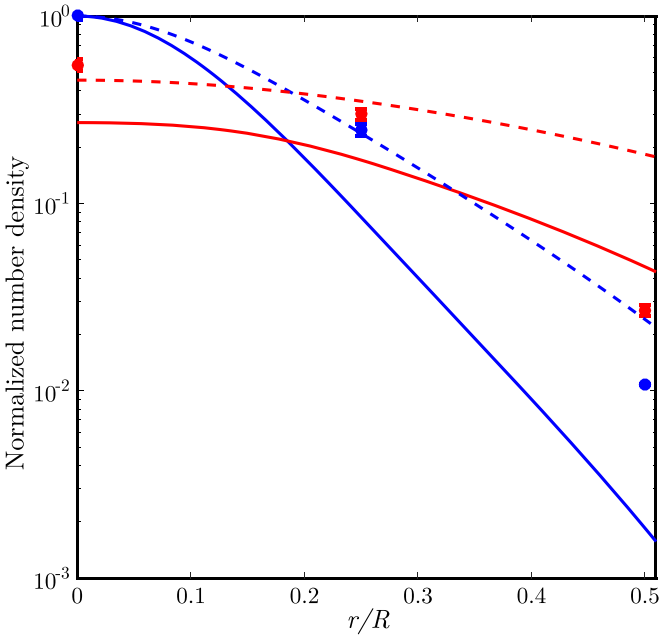

FIG. 7. Normalized number densities of Ar^+ and Ar_2^+. The blue and red solid lines are the Ar^+ and Ar_2^+ densities, respectively, calculated by means of the full model. The dashed blue and red curves are the Ar^+ and Ar_2^+ densities, respectively, obtained when the EEDF was assumed to be Maxwellian. The experimental values for Ar^+ (blue symbols) and Ar_2^+ (red symbols) are also shown [20].

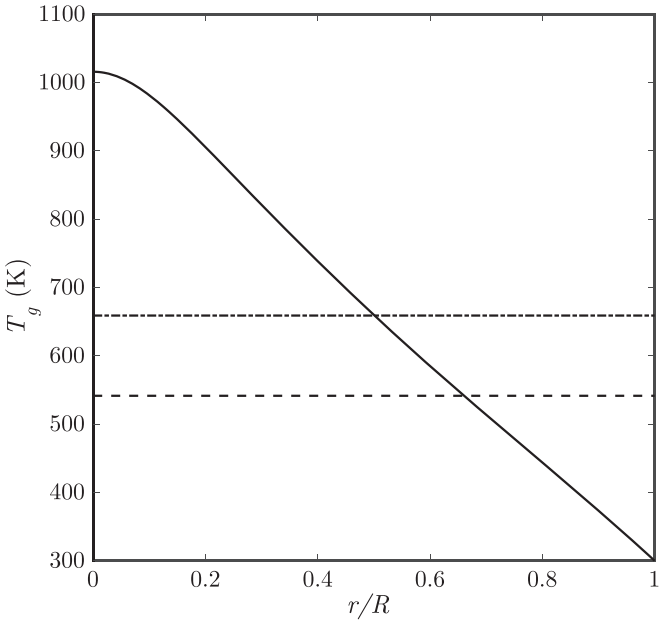

FIG. 8. Radial profile of the gas temperature (solid sloping curve), generated using the full model. The horizontal lines are used to display graphically the values of the calculated mean (dashed) and the measured (dot-dashed) temperatures, $\langle T_g \rangle$ and $T_{g,\mathrm{OH}}$, where $\langle T_g \rangle =$ 542 K and $T_{g,\mathrm{OH}} = 659(8)$ K.

both in the model and the experiment that may hinder the accuracy. For instance, we took a more or less arbitrary branching ratio for the dissociative recombination reaction. Since this parameter is critical, an error in the branching ratio could explain the observed discrepancies. On the experimental side, we must consider that the mass spectrometer's probe disturbs the discharge and it may actually change by a considerable amount the electron density at the column center and the electric field profile, even if all other physical conditions are kept fixed. Besides, the pure Ar plasma chemistry is disturbed by the presence of air molecules, whose effect is more important in the borders of the positive column. Therefore, we may consider a qualitative agreement to be the best achievable result.

For the sake of completeness, we also show the radial profile of the excited species $Ar(^3P_2)$, $Ar(^1P_1)$, $Ar(^3P_0)$, $Ar(^3P_1)$, $Ar(4p)$, and Ar_2^*. Note that the metastable $Ar(^3P_2)$ is the most abundant species in the discharge center. It has the highest statistical weight, which explains its high density relative to the other excited species. The relatively high density of the states in the $4s$ configuration explains why the main creation processes of electrons is the electronic impact ionization from these excited atoms. The $Ar(4p)$ states present only a negligible density along the radius. It is also interesting to note that the excimer profile is much broader relative to the other excited species. This may be explained by the fact that we considered that the excimer extinction occurs only via collision with other identical partners, electrons or $4s$ states. The density profile of these species always decreases radially, contrary to the argon ground state. The quench by argon atoms seems to be negligible [40] and it was not included in the model. If this behavior is confirmed experimentally, it may be explored to build new excimer laser sources.

2. Gas and electron temperature

The radial profile of the calculated gas temperature is shown in Fig. 8. A dashed horizontal line is used to show the mean value $\langle T_g \rangle = (2/R^2) \int T_g(r) r\, dr = 542$ K, which is compared to the value estimated by means of the Boltzmann plot of the line intensities from the OH ($A\,^2\Sigma^+, v' = 0 \rightarrow X\,^2\Pi, v'' = 0$) UV band, $T_{g,\mathrm{OH}} = 659(8)$ K [60]. The values are consistent and the difference may be explained by the fact that the OH radial profile may differ from the gas temperature radial profile. Besides, the rotational temperatures are generally higher than the gas temperature in nonequilibrium discharges [60,63].

Figure 9 shows the radial profiles of the reduced electric field and the electronic temperature. The reduced electric field decreases towards the border, even if the axial component of the electric field, E_z, increases. This happens because the gas density increases faster than the electric field. The electron temperature follows a similar trend, but it increases slightly between $r/R = 0$ and $r/R = 0.2$ and after that it decreases. We also included in the plot the "Thomson temperature," which allows us to compare our results with Thomson scattering temperature measurements [23]. The temperature measured by this technique is often considered the most accurate plasma diagnostic for electron temperature measurements. However, assumptions must be met, which is discussed next.

The Thomson scattering gives the profile of the light elastically scattered by electrons in the plasma column. If the EEDF is Maxwellian, this profile can be proven to have a Gaussian shape and an expression can be derived which relates the standard deviation with the electric temperature. However,

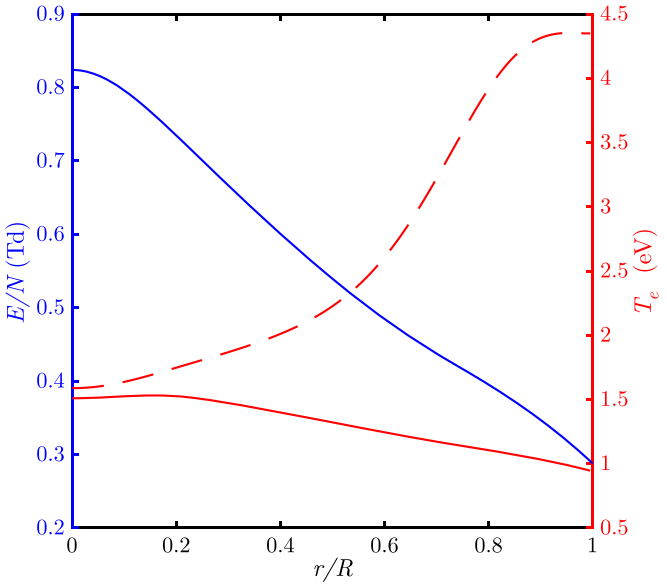

FIG. 9. Radial profiles of the reduced electric field E/N (blue solid line), electron temperature $T_e = 2/3\langle\epsilon\rangle$ (red solid line), and Thomson temperature $T_{e,th}$ (red dashed line). These quantities were derived from the full model results.

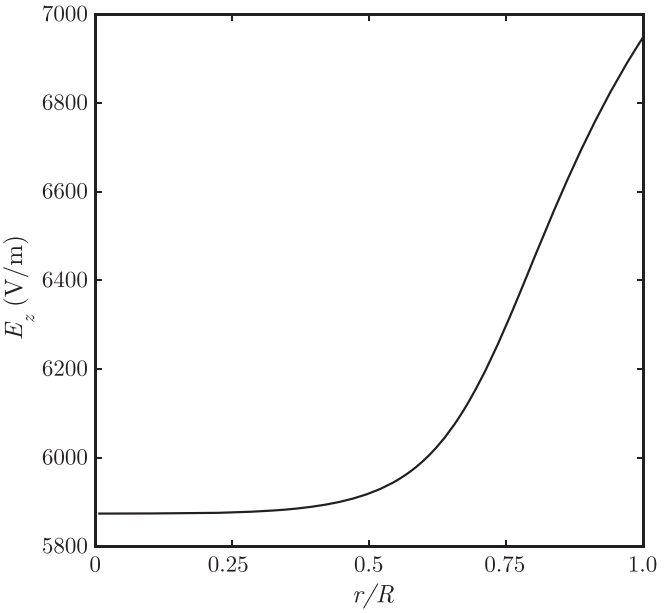

FIG. 10. Radial profile of the magnitude of the axial component of the electric field, E_z, obtained in the full model simulation.

if the EEDF is not Maxwellian, there is no guarantee that the Gaussian fit will actually give the real electron temperature, if it is defined as $T_e = 2/3\langle u\rangle$. In this case, the populous low energy electrons provide the most important contribution to the scattered light and the resulting profile is not exactly Gaussian. However, it is usually fitted as if it were a normal distribution and the electron temperature is derived in the usual manner. Actually, the deviation from a Gaussian is imperceptible, because the EEDF in the energy interval between 0 eV and 2 eV, which contains the electron population that gives the most important contribution for the light scattering, may be approximated by a straight line, even in the worst cases. The contribution of more energetic electrons ($u_e > 2$ eV) in the tail of the Doppler broadened scattering profile, which could possibly show the deviation from the equilibrium EEDF, is obscured by the signal noise [22]. That is why we may define the Thomson temperature as the temperature of the Maxwellian which best fits the nonequilibrium EEDF in the energy interval from 0 eV to 2 eV (see Fig. 12).

Using this definition, we clearly see that the Thomson temperature increases radially as observed experimentally [23]. Nonetheless, this is just an artifact caused by the increasingly higher deviation from equilibrium of the EEDF as the electron density decreases due to the column contraction. It has been often stated that the electron temperature "must increase" in order to keep the discharge alive, but this is not the case. Actually, one must analyze whether the physical conditions are such that the plasma existence is possible. Besides, real electron temperatures of 2 eV or 3 eV at the borders would result in very high ionization rates, causing the electron density at the borders to be higher than in the center in spite of the dissociative recombination. No stability would be possible in this case.

The radial profile of the magnitude of the axial component of the electric field, E_z, is shown in Fig. 10. The plot in Fig. 11 compares the radial profiles of the electron density, n_e, and the Thomson electron temperature, $T_{e,th}$. This plot is analogous to the one shown in [23], where both n_e and T_e were obtained experimentally in similar physical conditions by means of Thomson scattering. We were able to reproduce this apparent increase in the electronic temperature, but only using this new definition of the electron temperature.

The procedure used to obtain the Thomson electron temperature is shown in Fig. 12. The EEDFs in three different positions are shown: $r/R = 0.0$, $r/R = 0.25$, and $r/R = 0.5$. As the radial coordinate increases, the EEDF becomes more

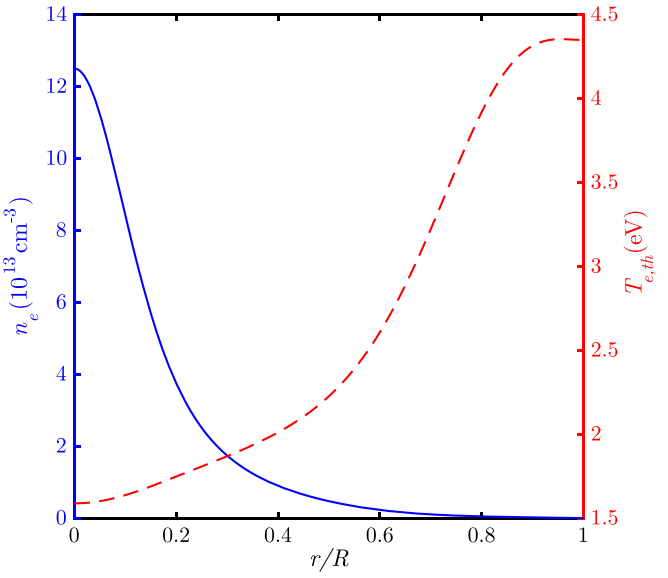

FIG. 11. Comparison between the radial profiles of the electron density, n_e, and the Thomson electron temperature, $T_{e,th}$. These quantities were derived from the full model results.

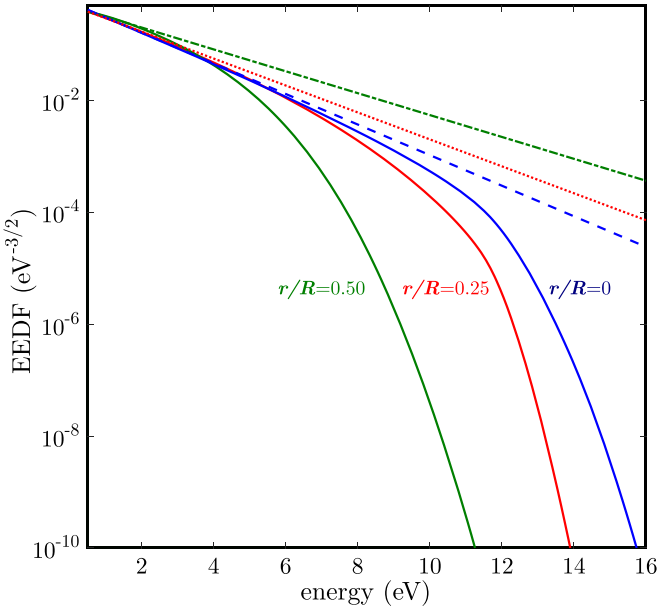

FIG. 12. Electron energy distribution functions at different radial coordinates: $r/R = 0$ mm (blue solid line), $r/R = 0.25$ mm (red solid line), and $r/R = 0.5$ mm (green solid line). The Maxwellian distribution which was fitted in the low energy electron interval is also shown: $r/R = 0$ mm (blue dashed line), $r/R = 0.25$ mm (red dotted line), and $r/R = 0.5$ mm (green dot-dashed line). The EEDFs were obtained using the full model simulation.

depleted due to the decrease of the electron density. Here we recall that the higher the electron density, the higher the *e*-*e* collisions rates, so that the EEDF is expected to approach equilibrium. Note that the nonequilibrium EEDF always exhibits a negative concavity on a logarithm scale. Consequently, the Thomson electron temperature is higher than the values of the real electron temperature. The concavity tends to increase as the EEDF deviates more and more from the equilibrium and this accounts for the apparent increase in temperature.

Lastly, we would like to discuss the impact of the EEDF on the ionization rate. As can be clearly seen in Fig. 12 the tail of the EEDF tends to be more and more depleted as the electron density decreases. This certainly would have a large impact on the rate coefficient of electronic ionization from the ground state, since the ionization threshold in this case is 15.6 eV and the EEDF experiences a drastic drop in the vicinity of this value. Nevertheless, the most important ionization source comes from the electron impact with excited states. In the case of the 4*s* states, the threshold value is approximately 4.0 eV. In the vicinity of this value, the tail depletion is much less pronounced and the effect on the ionization rate coefficient will be relatively small. This reinforces our prior conclusion: the contraction phenomena is more related to the dissociative recombination than to the nonequilibrium EEDF. It also explains why the models which considered the EEDF to be Maxwellian could provide reasonable results. This conclusion should be valid not only to atmospheric pressure plasmas, but also to intermediate pressure discharges where the transition from single-step to multistep ionization occurs before plasma contraction. On the other hand, if single-step ionization is the main creation mechanism or no dissociative recombination occurs in a particular discharge configuration where the constriction is experimentally observed, then other explanations based on the nonequilibrium EEDF would be more appropriate.

IV. CONCLUSION

In this work we reported a physical model for the description of an argon discharge sustained by surface waves at atmospheric pressure. We focused on the problem of column contraction and we elucidated the relative importance of the dissociative recombination and the nonequilibrium EEDF to the onset of this phenomenon. By detailed examination of our results, which also included two alternative scenarios where the dissociative recombination was switched off and the EEDF was considered to be Maxwellian, the dissociative recombination was shown to be the most important process leading to plasma contraction. The leading charge creation path was ionization from the excited species, mainly the 4*s* states and the molecular argon excimer. Although the EEDF exhibited a significant tail depletion in the region of the column borders where the electron density was relatively small, it was not pronounced enough to produce a significant change in the rate coefficients of the previously mentioned processes, which have low ionization thresholds. The dissociative recombination proved to be the most important ingredient for the maintenance of the contracted discharge. The three-body atomic conversion is also an integral part of the constriction process, since without this process no molecular ion would be formed. The nonhomogeneous heating is essential, since it causes a positive density gradient of neutral atoms which contributes to the maintenance of the molecular ion formation in the borders. However, the nonhomogeneous heating only aids the contraction; the dissociative recombination could possibly cause contraction even if the atomic density were uniform.

The simulation results showed that the density of the molecular ion Ar_2^+ becomes larger than that of the atomic ion Ar^+ at the borders of the plasma column. This behavior was predicted by Kenty [5] and it was verified experimentally recently [20]. Another important contribution of this work was the elucidation of the apparent steep electron temperature increase towards the border which was observed in Thomson scattering plasma diagnostics. We showed that our results can reproduce this behavior if the effect of the nonequilibrium EEDF is taken into account in the interpretation of the electron temperature measured by Thompson scattering.

ACKNOWLEDGMENTS

M.A.R. would like to thank the Brazilian National Council for the Improvement of Higher Education for the scholarship under Grant No. CAPES/ITA 005/2014 which enabled him to focus on the development of the plasma modeling code and complete this work. J.A. would like to thank the Brazilian National Council for the Improvement of Higher Education for the financial support under Grant No. CAPES/ITA 035/2013. G.P. was supported by the Naval Research Laboratory 6.1 Base Program. V.G. was partially supported by the Portuguese FCT under Project No. UID/FIS/50010/2013.

[1] J. Stark, *Die Elektrizität in Gasen* (J.A. Barth, Leipzig, 1902).
[2] W. Schottky, Z. Phys. **25**, 635 (1924).
[3] R. Fowler, Proc. Phys. Soc. London, Sect. B **68**, 130 (1955).
[4] W. P. Allis and D. J. Rose, Phys. Rev. **93**, 84 (1954).
[5] C. Kenty, Phys. Rev. **126**, 1235 (1962).
[6] W. Elenbaas, *The High Pressure Mercury Vapour Discharge*, Vol. 2 (North-Holland Publishing Company, Amsterdam, 1951).
[7] W. H. Bennett, Phys. Rev. **45**, 890 (1934).
[8] Y. B. Golubovskii and R. Sonneburg, Sov. Phys. Tech. Phys. **49**, 295 (1979).
[9] Y. Golubovskii and R. Sonneburg, Sov. Phys. Tech. Phys. **49**, 302 (1979).
[10] Y. Golubovskii and R. Sonneburg, Sov. Phys. Tech. Phys. **49**, 754 (1979).
[11] Y. B. Golubovskii, V. Nekuchaev, S. Gorchakov, and D. Uhrlandt, Plasma Sources Sci. Technol. **20**, 053002 (2011).
[12] Y. Golubovskii, D. Kalanov, and V. Maiorov, Phys. Rev. E **96**, 023206 (2017).
[13] E. Castanos Martinez, Y. Kabouzi, K. Makasheva, and M. Moisan, Phys. Rev. E **70**, 066405 (2004).
[14] Y. Kabouzi, D. B. Graves, E. Castaños-Martínez, and M. Moisan, Phys. Rev. E **75**, 016402 (2007).
[15] G. M. Petrov and C. M. Ferreira, Phys. Rev. E **59**, 3571 (1999).
[16] N. Dyatko, Y. Z. Ionikh, I. Kochetov, D. Marinov, A. Meshchanov, A. Napartovich, F. Petrov, and S. Starostin, J. Phys. D **41**, 055204 (2008).
[17] J. Gregório, P. Leprince, C. Boisse-Laporte, and L. Alves, Plasma Sources Sci. Technol. **21**, 015013 (2012).
[18] M. Jimenez-Diaz, E. Carbone, J. Van Dijk, and J. Van der Mullen, J. Phys. D **45**, 335204 (2012).
[19] M. Baeva, A. Bösel, J. Ehlbeck, and D. Loffhagen, Phys. Rev. E **85**, 056404 (2012).
[20] M. Ridenti, N. Spyrou, and J. Amorim, Chem. Phys. Lett. **595**, 83 (2014).
[21] E. Carbone, S. Hübner, J. Palomares, and J. Van der Mullen, J. Phys. D **45**, 345203 (2012).
[22] E. Carbone, S. Hübner, M. Jimenez-Diaz, J. Palomares, E. Iordanova, W. Graef, A. Gamero, and J. van der Mullen, J. Phys. D **45**, 475202 (2012).
[23] A. Van Gessel, E. Carbone, P. Bruggeman, and J. Van der Mullen, Plasma Sources Sci. Technol. **21**, 015003 (2012).
[24] M. Moisan, C. Beaudry, and P. Leprince, IEEE Trans. Plasma Sci. **3**, 55 (1975).
[25] C. Tendero, C. Tixier, P. Tristant, J. Desmaison, and P. Leprince, Spectrochim. Acta, Part B **61**, 2 (2006).
[26] P. M. Morse, W. Allis, and E. Lamar, Phys. Rev. **48**, 412 (1935).
[27] H. Margenau, Phys. Rev. **69**, 508 (1946).
[28] T. Holstein, Phys. Rev. **70**, 367 (1946).
[29] M. Bayet, J.-L. Delcroix, and J.-F. Denisse, J. Phys. Radium **15**, 795 (1954).
[30] G. Colonna and A. D'Angola, *Plasma Modeling* (IOP Publishing, Bristol, UK, 2016).
[31] R. D. White, R. E. Robson, B. Schmidt, and M. A. Morrison, J. Phys. D **36**, 3125 (2003).
[32] Z. L. Petrović, S. Dujko, D. Marić, G. Malović, Ž Nikitović, O. Šašić, J. Jovanović, V. Stojanović, and M. Radmilović-Radenović, J. Phys. D **42**, 194002 (2009).
[33] W. P. Allis, *Motions of Ions and Electrons*, Handbuch der Physik, Vol. 21 (Springer, Berlin, 1956).
[34] C. M. Ferreira and J. Loureiro, Plasma Sources Sci. Technol. **9**, 528 (2000).
[35] J. Loureiro and J. Amorim, *Kinetics and Spectroscopy of Low Temperature Plasmas* (Springer, Berlin, 2016).
[36] L. Vriens and A. H. M. Smeets, Phys. Rev. A **22**, 940 (1980).
[37] L. Alves and C. Ferreira, IST-Lisbon database, www.lxcat.net, retrieved May 15, 2014.
[38] O. Klein and S. Rosseland, Z. Phys. **4**, 46 (1921).
[39] M. A. Ridenti, V. Guerra, and J. Amorim, in *Plasma Modeling*, edited by G. Colonna and A. D'Angola (IOP Publishing, Bristol, UK, 2016), Chap. 11.
[40] S. K. Lam, C.-E. Zheng, D. Lo, A. Dem'yanov, and A. P. Napartovich, J. Phys. D **33**, 242 (2000).
[41] G. M. Petrov and C. M. Ferreira, arXiv:1308.2593.
[42] K. Kutasi, V. Guerra, and P. Sá, J. Phys. D **43**, 175201 (2010).
[43] J. Jonkers, M. van de Sande, A. Sola, A. Gamero, and J. van der Mullen, Plasma Sources Sci. Technol. **12**, 30 (2003).
[44] W. L. Wiese, J. W. Brault, K. Danzmann, V. Helbig, and M. Kock, Phys. Rev. A **39**, 2461 (1989).
[45] J. D. C. Jones, D. G. Lister, D. P. Wareing, and N. D. Twiddy, J. Phys. B **13**, 3247 (1980).
[46] T. F. O'Malley, A. J. Cunningham, and R. M. Hobson, J. Phys. B **5**, 2126 (1972).
[47] H. Brunet, B. Lacour, J. Rocca Serra, M. Legentil, S. Mizzi, S. Pasquiers, and V. Puech, J. Appl. Phys. **68**, 4474 (1990).
[48] J. Jonkers, M. van de Sande, A. Sola, A. Gamero, A. Rodero, and J. van der Mullen, Plasma Sources Sci. Technol. **12**, 464 (2003).
[49] A. Dalgarno, Philos. Trans. R. Soc. London A **250**, 426 (1958).
[50] T. Holstein, Phys. Rev. **83**, 1159 (1951).
[51] W. F. Liu and D. C. Conway, J. Chem. Phys. **62**, 3070 (1975).
[52] D. Smith, A. G. Dean, and I. C. Plumb, J. Phys. B **5**, 2134 (1972).
[53] P. Lukáč, O. Mikuš, I. Morva, Z. Zábudlá, J. Trnovec, and M. Morvová, Plasma Sources Sci. Technol. **20**, 055012 (2011).
[54] G. B. Ramos, M. Schlamkowitz, J. Sheldon, K. A. Hardy, and J. R. Peterson, Phys. Rev. A **51**, 2945 (1995).
[55] V. Marchenko, J. Exp. Theor. Phys. **85**, 510 (1983).
[56] C. Knopp and A. B. Cambel, Phys. Fluids **9**, 989 (1966).
[57] B. Younglove and H. J. Hanley, J. Phys. Chem. Ref. Data **15**, 1323 (1986).
[58] I. Zhelyazkov and E. Benova, J. Appl. Phys. **66**, 1641 (1989).
[59] J. A. Bittencourt, *Fundamentals of Plasma Physics* (Springer Science & Business Media, Berlin, 2013).
[60] M. A. Ridenti, J. A. Souza-Corrêa, and J. Amorim, J. Phys. D **47**, 045204 (2014).
[61] J. Amorim, M. A. Ridenti, and V. Guerra, Plasma Phys. Controlled Fusion **57**, 074001 (2015).
[62] M. A. Ridenti, Diagnóstico e modelagem de plasmas gerados por micro-ondas e aplicações, Ph.D. thesis, State University of Campinas, 2014.
[63] P. Bruggeman, D. C. Schram, M. G. Kong, and C. Leys, Plasma Proces. Polym. **6**, 751 (2009).